JACS
JOURNAL OF THE AMERICAN CHEMICAL SOCIETY

ARTICLE

pubs.acs.org/JACS

Activation of α-Keto Acid-Dependent Dioxygenases: Application of an $\{FeNO\}^7/\{FeO_2\}^8$ Methodology for Characterizing the Initial Steps of O_2 Activation

Adrienne R. Diebold,[‡] Christina D. Brown-Marshall,[‡] Michael L. Neidig,[‡] June M. Brownlee,[§] Graham R. Moran,[§] and Edward I. Solomon*[,‡,†]

[‡]Department of Chemistry, Stanford University, Stanford, California 94305, United States

[†]Stanford Synchrotron Radiation Lightsource, SLAC, Stanford, California 94309, United States

[§]Department of Chemistry and Biochemistry, University of Wisconsin—Milwaukee, Milwaukee, Wisconsin 53211, United States

Supporting Information

ABSTRACT: The α-keto acid-dependent dioxygenases are a major subgroup within the O_2-activating mononuclear nonheme iron enzymes. For these enzymes, the resting ferrous, the substrate plus cofactor-bound ferrous, and the Fe^{IV}=O states of the reaction have been well studied. The initial O_2-binding and activation steps are experimentally inaccessible and thus are not well understood. In this study, NO is used as an O_2 analogue to probe the effects of α-keto acid binding in 4-hydroxyphenylpyruvate dioxygenase (HPPD). A combination of EPR, UV—vis absorption, magnetic circular dichroism (MCD), and variable-temperature, variable-field (VTVH) MCD spectroscopies in conjunction with computational models is used to explore the HPPD—NO and HPPD—HPP—NO complexes. New spectroscopic features are present in the α-keto acid bound $\{FeNO\}^7$ site that reflect the strong donor interaction of the α-keto acid with the Fe. This promotes the transfer of charge from the Fe to NO. The calculations are extended to the O_2 reaction coordinate where the strong donation associated with the bound α-keto acid promotes formation of a new, $S = 1$ bridged Fe^{IV}—peroxy species. These studies provide insight into the effects of a strong donor ligand on O_2 binding and activation by Fe^{II} in the α-keto acid-dependent dioxygenases and are likely relevant to other subgroups of the O_2 activating nonheme ferrous enzymes.

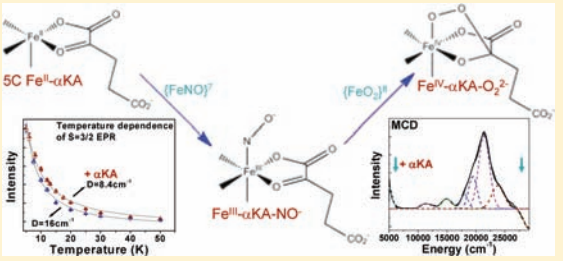

INTRODUCTION

The mononuclear nonheme iron enzymes catalyze a diverse range of chemical reactions that include dioxygenation, hydroxylation, ring closure, oxidative desaturation, carbon—carbon bond and aromatic ring cleavage, and halogenation.[1−8] Within this broad class, the oxygen-activating enzymes use an Fe^{II} center to activate triplet dioxygen for the formally spin-forbidden reaction with organic substrates. These include the α-keto acid-dependent dioxygenases. These enzymes use an α-keto acid group as a cosubstrate, providing electrons for dioxygen cleavage.[1,4,5,9] A general mechanistic strategy (Scheme 1) has been developed in which the binding of both the α-keto acid group and the substrate results in an open coordination position on the Fe^{II} for O_2 activation.[1] Reaction with O_2 leads to decarboxylation of the α-keto acid and generation of a highly reactive Fe^{IV}=O species. This Fe^{IV}=O species then undergoes an electrophilic reaction with the substrate.[1,4,5,8,10−13] The binding of both the substrate and the α-keto acid and the reactive nature of the Fe^{IV}=O species have been extensively studied.[2−4,8,12,14] The initial O_2 binding and activation steps, however, have not been definitively observed and therefore are not well understood.

As no O_2 intermediate prior to the Fe^{IV}=O species has been experimentally trapped in the α-keto acid-dependent dioxygenases, other approaches to probe these initial steps must be taken. NO binds to ferrous sites;[15−20] however, it is one electron deficient with respect to O_2 and does not react further. These complexes are described as $\{FeNO\}^7$ following the notation of Enemark and Feltham[21] where the superscript refers to the total number of Fe d plus NO valence electrons (6 electrons from the ferrous site and one from NO). These $\{FeNO\}^7$ complexes are stable and chromophoric with half-integer spin (typically $S = 3/2$),[15,18] making them good spectral probes and amenable to study by electron paramagnetic resonance (EPR), UV—visible absorption, and magnetic circular dichroism (MCD) spectroscopies. Initial studies on the Fe—EDTA—NO complex showed an $S = 3/2$ site (from EPR) with intense charge transfer transitions in the UV—vis absorption and MCD spectra (Supporting Information Figures S2, S3A). XAS and resonance Raman studies assigned the electronic structure of the $\{FeNO\}^7$ unit as high spin Fe^{III} ($S = 5/2$) antiferromagnetically coupled to NO^- ($S = 1$).[22] Computational modeling supported this description giving an Fe^{III}—NO^- electronic structure characterized by 5 unoccupied β Fe d orbitals

Received: March 21, 2011
Published: October 08, 2011

Scheme 1. Proposed Mechanism for α-Keto Acid-Dependent Dioxygenases (Adapted from Ref 1)

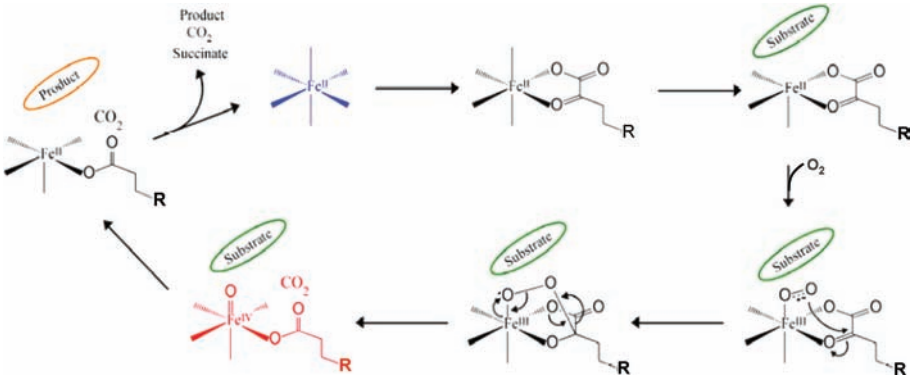

Scheme 2. Reaction Catalyzed by HPPD

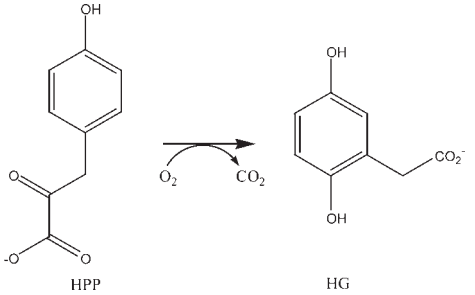

and 2 unoccupied α NO^{-} orbitals.[22−24] The $\{FeNO\}^7$ computational description was then extended to provide experimentally calibrated models for $\{FeO_2\}^8$.[23] This $\{FeNO\}^7/\{FeO_2\}^8$ methodology was used to characterize the initial steps of the O_2 reaction of Isopenicillin *N* Synthase (IPNS).[25] In that study, the $\{FeNO\}^7$ complex provided an understanding of the effect of the native substrate (δ-(L-α-aminoadipoyl)-L-cysteinyl-D-valine, ACV) coordination to the Fe through its thiolate ligand. Extension of the experimentally calibrated $\{FeNO\}^7$ description to an $\{FeO_2\}^8$ computational model led to a FeIII-superoxide frontier molecular orbital for H-atom abstraction (the first O_2-dependent step of the mechanism). The results for IPNS show the utility of the $\{FeNO\}^7/\{FeO_2\}^8$ methodology in evaluating the initial steps of the O_2 reaction.

The present study focuses on the α-keto acid-dependent dioxygenase, (4-hydroxyphenyl)pyruvate dioxygenase (HPPD). HPPD catalyzes the reaction of (4-hydroxyphenyl)pyruvate (HPP) with dioxygen to release CO_2 and the product, homogentisate (Scheme 2).[26] HPPD has been chosen for this study because the resting ferrous and ES complexes have been studied previously.[27−29] Additionally, in HPP the α-keto acid moiety is fused to the substrate facilitating formation of the catalytically relevant ES complex. From our previous study of the ferrous ES complex,[29] there is less MCD intensity from the ligand field transition of the Fe site at low energy (relative to other α-keto acid-dependent dioxygenases), which facilitates a clear assignment of a new low energy transition present in the MCD spectrum of the HPPD−HPP−NO complex (vide infra).

This study examines the effect of the α-keto acid binding to the $\{FeNO\}^7$ unit. The NO-bound complexes of both resting HPPD and HPPD−HPP are studied, where the HPPD−NO complex provides a reference to define the new features that arise from the bound α-keto acid in the HPPD−HPP−NO complex. The experimental study of the HPPD−NO and HPPD−HPP−NO complexes is then extended to computational models. To obtain a general picture of α-keto acid nonheme Fe reactivity and to compare to the published literature, the computational model presented in this study is an Fe^{II} α-ketoglutarate-bound facial triad. However, the key computational steps have also been evaluated with HPP as the substrate and are presented in the Supporting Information. Analysis of the $\{FeNO\}^7$ computational models in conjunction with the experimental HPPD−(HPP)−NO data leads to an understanding of the effects of the α-keto acid on the $\{FeNO\}^7$ bond. Insight gained from the $\{FeNO\}^7$ complex is extended to the mechanistically relevant $\{FeO_2\}^8$ complex. Evaluation of the $\{FeO_2\}^8$ complex and the subsequent reaction coordinate allows an evaluation of proposed mechanisms of reactivity and provides insight into the initial steps of the O_2 reaction in the α-keto acid-dependent dioxygenases leading to the formation of the Fe^{IV}═O intermediate for subsequent reaction with substrate.

2. MATERIALS AND METHODS

HPPD was purified according to previously published procedures.[26] Apo-HPPD was exchanged into 50 mM 2-[4-(2-hydroxyethyl)-piperazin-1-yl]ethanesulfonic acid (HEPES) buffer in D_2O at a pD of 7.1 using an Ultrafree-4 filter with a 10 kDa cutoff membrane (Millipore) to a concentration of 2−4 mM. All other reagents were used as received without further purification. Buffer, HPP, ferrous ammonium sulfate, methyl-[6-[methyl-[nitroso(oxido)amino]amino]hexyl]azanium (NONOate), and glycerol were made anaerobic by purging with Ar on a Schlenk line. HPPD was made anaerobic by alternating cycles of vacuum and purging with Ar at 273 K. All samples for spectroscopy were prepared in an inert atmosphere, N_2-purged "wet box" to maintain an O_2-free environment. Ferrous ammonium sulfate was dissolved in buffer and added to HPPD in microliter quantities to a concentration of 90% of the enzyme (monomer) concentration to avoid free iron in the sample. HPP was added to buffer to form a saturated solution. Residual solid HPP was filtered out of the solution, and the concentration of the HPP solution was determined from the intensity of the 270 nm maximum in the absorption spectrum. For the substrate-bound samples, HPP was added in microliter quantities to a concentration of 5−10 times the concentration of the protein. Solid NONOate was dissolved in 220 mM NaOH for a final concentration of 90 mM and added to the HPPD−Fe^{II} and HPPD−Fe^{II}−HPP solutions in microliter quantities to a concentration of ∼2 times the concentration of the protein. Glycerol

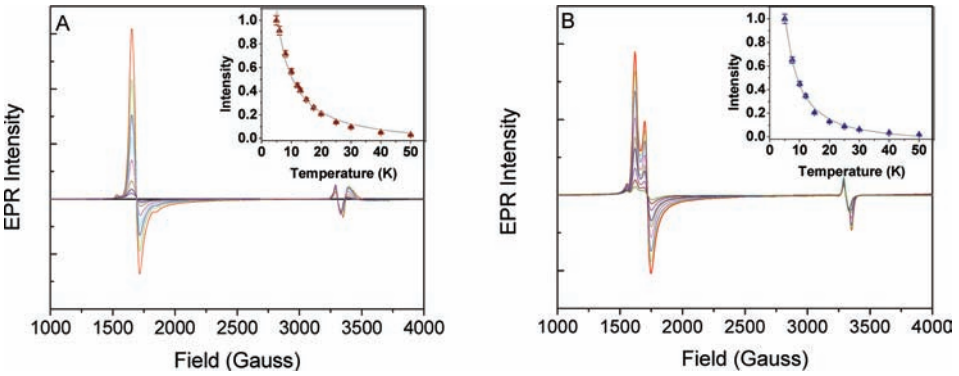

Figure 1. EPR of $\{FeNO\}^7$ enzyme complexes. EPR of $S = 3/2$ HPPD−NO (A) and HPPD−HPP−NO (B) showing the inverse temperature dependence of the signal intensity. The inlays show the best fit to the data.

(∼50−60% v/v) was added as a glassing agent to samples for MCD. CD control experiments showed no effect of the glycerol on the Fe site.

NIR (600−2000 nm) MCD spectra were taken on either a Jasco J-200D or a Jasco J-730 spectropolarimeter with a liquid N_2 cooled InSb detector (Teledyne Judson Technologies) and an Oxford Instruments SM-4000-7T superconducting magnet. UV−vis (300−900 nm) MCD spectra were taken on a Jasco J-810D spectropolarimeter equipped with an extended S20 photomultiplier tube and a SM-4000-7T superconducting magnet. UV−vis absorption spectra were taken on an Agilent 8453 diode array spectrometer. Absorption spectra were taken at 278 K in an anaerobic cuvette and were corrected for buffer and protein baseline effects by subtraction. Natural CD features and baseline effects were eliminated from the MCD spectra by taking one-half the difference of positive and negative field data. For VTVH MCD, a calibrated Cernox resistor (Lakeshore Cryogenics, calibrated 1.5−300 K), inserted into the sample cell, was used for accurate temperature measurement. The VTVH MCD data obtained were normalized to the intensity maximum. X-band EPR spectra were taken on a Bruker EMX spectrometer with a Bruker ER 041XG/ER microwave bridge and ER 4102ST/ER 5106QT cavity. Spectra were taken at temperatures between 3.8 and 50 K using an Oxford ITC503 temperature controller with an ESR 900 continuous flow cryostat.

The computational models for the resting enzyme plus NO (E−NO) and the α-keto acid bound enzyme plus NO (E−αKA−NO) were taken from the CS2-α-ketoglutarate-NO crystal structure (PDB entry: 1gvg). Histidine residues were truncated to methyl imidazole, and glutamate was truncated to propionate for the models. Constraints imposed by the protein backbone were simulated in both computational models by fixing the relative positions of the β-carbons of the backbone.

Density functional theory (DFT) calculations were performed with the Gaussian 03 program[30,31] with the unrestricted BP86 functional[32] with 10% Hartree−Fock Exchange under tight convergence criteria. The Pople triple-ζ basis set, 6-311G*, was used to describe Fe, NO/O_2, and the α-keto acid moiety ($OCCO_2$). The double-ζ basis set, 6-31G*, was used for all other atoms. This method has been calibrated previously for $\{FeNO\}^7$ complexes.[23] For comparison with literature results, calculations were also performed with the unrestricted B3LYP functional under tight convergence criteria. The LANL2DZ effective core potential basis set was used in these to describe the Fe, and the Pople double-ζ basis set, 6-31G, was used to describe all other atoms. All structures were optimized and found to be stable with no imaginary frequencies < i15 cm^{-1} (which are associated with the constraints placed on the β-carbons). Effects of the protein environment were included by applying the polarized continuum model (PCM)[33] with a dielectric constant, $\varepsilon = 4.0$, to calculate solvated energies for the complexes. These solvated single point calculations were done with the 6-311+G(2d,p) basis set. (For the B3LYP models, the 6-311G** basis set was used, consistent with literature.[34,35]) The energies given include thermal and zero-point corrections. As the Gaussian package does not allow for ΔSCF calculations (convergence of a wave function in a user-defined excited state), the Amsterdam Density Function (ADF 2010.02) package[36−38] was used to calculate the ΔSCF excitations. Using the Gaussian 03-optimized geometries, excited states for the ligand field transitions were calculated with the unrestricted BP86 functional with the uncontracted triple-ζ basis set (TZP) with a single polarization function without a frozen core approximation. To allow for differences between the pure functional and hybrid calculations, the Z of Fe was set to 25.6 (single point calculation) as was previously calibrated for similar calculations on $\{FeNO\}^7$ model complexes.[23] All excitations were calculated as Slater transition states. ZFS parameters were calculated in ORCA (version 2.8) for both models using the B1P functional with 10% H−F exchange and with the CP(PPP) basis set on Fe, TZVP on N and O, and SVP on all other atoms.[39] Structures were visualized with GaussView 3.09;[40] orbital compositions were determined with QMForge;[41] and molecular orbitals were visualized with Molden version 4.1.[42] Time-dependent DFT (TD-DFT) calculations were performed (with Gaussian 03 using BP86 with 10% HF exchange and the split 6-311G*/6-31G* basis set as described above) to compare to the experimental spectra, and SWizard was used to parse the results.[43,44]

3. RESULTS

3.1. Spectroscopic. Addition of NO to the resting, Fe^{II}-bound form of HPPD results in the EPR spectrum shown in Figure 1A. The HPPD−NO complex exhibits effective g' values of 3.96 and 2.00, indicating that it is a close to axial $S = 3/2$ species with an $E/D = 0.008$. A plot of the temperature dependence of the EPR signal intensity under nonsaturating conditions is shown as an inset in Figure 1A and in Supporting Information Figure S1 (red). Addition of NO to HPP bound Fe−HPPD results in the EPR spectrum shown in Figure 1B. The EPR signal of the HPPD−HPP−NO complex indicates that the spin of the ground state is still $S = 3/2$ but with $g_x' = 4.14$ and $g_y' = 3.90$ giving an E/D of 0.02. The inverse dependence of the EPR intensity with increasing temperature for the HPPD−HPP−NO spectrum is shown as an inset in Figure 1B and in Supporting Information Figure S1 (blue).

These EPR spectra are described by the spin Hamiltonian given in eq 1, where $g_0 = 2.0$ and D and E are the axial and rhombic ZFS parameters, respectively.[45]

$$\hat{H}_{spin} = D[S_z^2 - 5/4 + E/D(S_x^2 - S_y^2)] + g_0\beta \vec{S} \cdot \vec{H} \quad (1)$$

This splits the $S = 3/2$, $M_s = \pm 1/2, \pm 3/2$ by an amount $2D$. The inverse temperature dependence of the EPR signal intensity indicates that D is positive with $M_s = \pm 1/2$ lowest and is fit to a Boltzmann population of the Curie law dependence (eq 2 where C is the Curie constant, T is the temperature in Kelvin, and k is the Boltzmann constant).

$$\text{intensity} = \frac{C}{T}\left[\frac{1}{1 + \exp(-2D/kT)}\right] \quad (2)$$

For the HPPD−NO EPR sample, this gives $D = 16 \pm 2$ cm^{-1}, while for the HPPD−HPP−NO sample, the value of the axial ZFS parameter has decreased to $D = 8.4 \pm 0.7$ cm^{-1}.

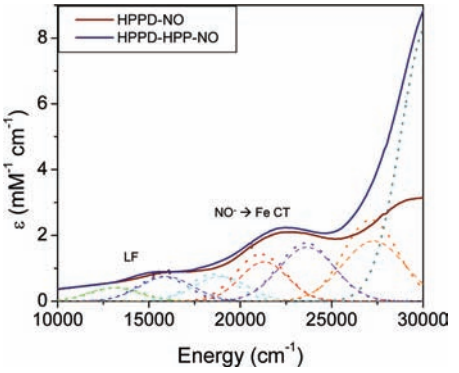

Figure 2. Room-temperature UV−vis absorption spectra of HPPD−NO (red) and HPPD−HPP−NO (blue). Gaussian resolution of the bands is shown (dashed for HPPD−NO and dotted for HPPD−HPP−NO).

The room-temperature UV−vis absorption spectra of the HPPD−NO and HPPD−HPP−NO complexes are shown in Figure 2 (with the Gaussian resolutions of the bands from a simultaneous fit with the MCD spectra presented below). The two spectra are very similar up to 25 000 cm^{-1}. However, a new intense transition resulting from HPP binding is observed above 25 000 cm^{-1}. The Fe−EDTA−NO complex has been extensively studied and provides a point of reference for this study.[22] The HPPD−NO UV−vis absorption spectrum is very similar to that of Fe−EDTA−NO (Supporting Information Figure S2). For the Fe−EDTA−NO complex, the two sets of bands observed are assigned as ligand-to-metal charge transfer transitions from NO$^-$ to Fe^{III} d (at 20 000−25 000 cm^{-1}) and Fe^{III} ligand field (LF) transitions (at ∼15 000 cm^{-1}).

The 5 K, 7 T MCD spectra of the HPPD−NO and HPPD−HPP−NO complexes are shown in Figure 3. The MCD spectra of these two complexes are generally similar with only small differences in energy and intensity of the major features. (The starred feature in the HPPD−NO MCD spectrum is due to unreacted resting HPPD.) The major differences between the MCD spectra of the resting and substrate-bound NO complexes are the new bands at low energy (<5000 cm^{-1}) and at high energy (∼29 000 cm^{-1}, negative MCD intensity) in the HPPD−HPP−NO complex in Figure 3B. The Gaussian resolutions of the bands in the two MCD spectra are also included in Figure 3. The MCD spectrum of HPPD−NO is very similar to that observed for the Fe−EDTA−NO complex (compare Gaussian resolutions in Supporting Information Figure S3 including tabulated transition energies). From the strong spectral correlation of Fe−EDTA−NO and HPPD−NO in absorption, MCD, and VTVH MCD (vide infra − the

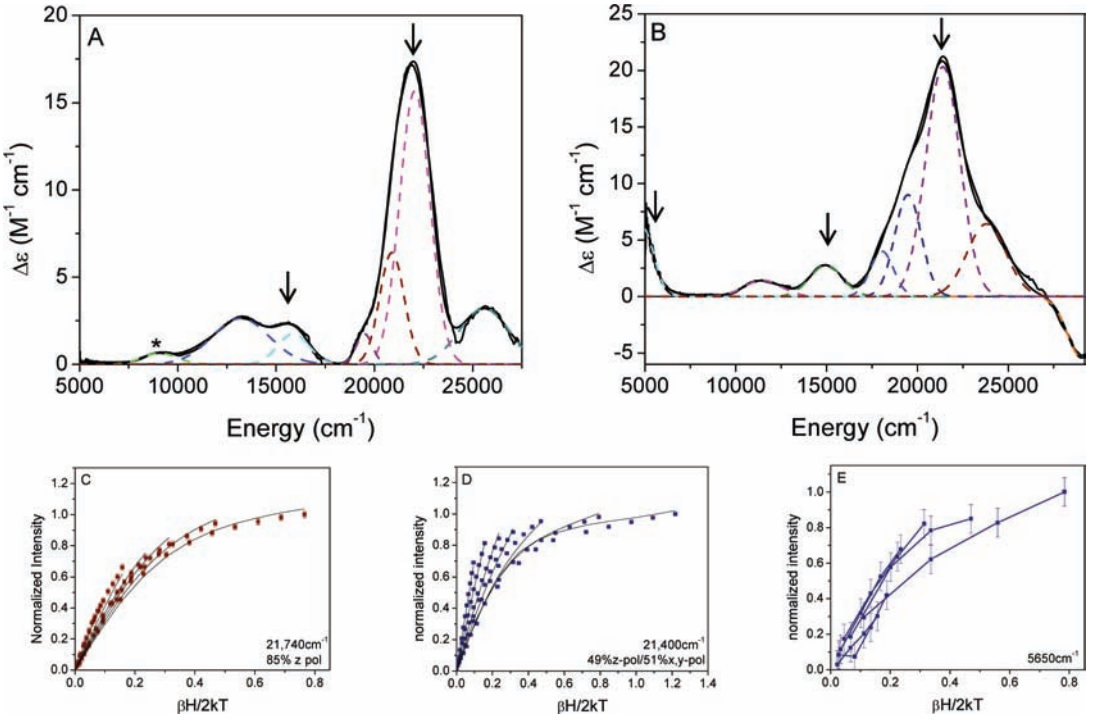

Figure 3. VTVH MCD of {FeNO}^{7}. (A,B) The 5 K, 7 T MCD spectra of HPPD−NO (A) and HPPD−HPP−NO (B). The Gaussian fits to the spectra are shown. For HPPD−NO, the star indicated unreacted resting HPPD. VTVH MCD isotherms were taken at the points indicated with arrows on the spectra of HPPD−NO and HPPD−HPP−NO. (C−E) The VTVH MCD isotherms and best fits to the data. (Data were collected at 1.8, 3, 5, 7.5, 10, 15, and 25 K for (C) and (D) and at 3, 5, 7.5, 12, and 15 for (E).) VTVH MCD taken for HPPD−NO at 21 700 cm^{-1} (C) and HPPD−HPP−NO at 21 400 cm^{-1} (D) and 5650 cm^{-1} (E).

dx.doi.org/10.1021/ja202549q |J. Am. Chem. Soc. 2011, 133, 18148–18160

transition at ~22 000 cm^{-1} in Fe−EDTA−NO is also *z* polarized, data not shown), the three transitions at ~18 000−24 000 cm^{-1} of the HPPD−NO complex are assigned as NO^- $2\pi^*$ to Fe^{III} d_π charge transfer transitions, while the two lower energy transitions are assigned as two of the Fe^{III} ligand field transitions (which are formally spin forbidden, but gain intensity through spin−orbit coupling with the nearby charge transfer transitions, vide infra). For the MCD spectrum of the HPPD−HPP−NO complex, the three transitions at ~17 000−25 000 cm^{-1} are also assigned as NO^- to Fe^{III} d charge transfer excitations, and the two lower energy transitions at 11 500 and 15 000 cm^{-1} are assigned as Fe^{III} ligand field transitions. This assignment is consistent with spin-forbidden ΔSCF calculations and TD-DFT calculations (see section 4.1). The transition at ~29 000 cm^{-1} corresponds to the new feature in the absorption spectrum of HPPD−HPP−NO. Assignment of the <5000 and 29 000 cm^{-1} transitions in the HPPD−HPP−NO complex will be considered in the analysis. VTVH MCD data give the polarizations of the transitions observed in Abs/MCD spectra.[46] The arrows in Figure 3 indicate the energies at which the VTVH MCD isotherms were taken to evaluate the polarizations of the corresponding transitions (energy positions where the associated Gaussian shows little overlap with other transitions). The VTVH MCD isotherms for the 21 700 cm^{-1} transition in HPPD−NO are shown in Figure 3C. The VTVH MCD for the ligand field transitions taken at 15 100 cm^{-1} is shown in Supporting Information Figure 4A. These isotherms were taken on the less intense ligand field transition to avoid any contribution to the VTVH MCD isotherms from the residual resting HPPD (which has negative MCD intensity in this region). For the HPPD−HPP−NO complex, VTVH MCD isotherms were taken at 21 400 cm^{-1} (Figure 3D), at 15 000 cm^{-1} for the ligand field transition (Supporting Information Figure S4B), and at 5650 cm^{-1} for the low energy transition (Figure 3E, the large error bars reflect the noise at this limit of our accessible spectral region). These VTVH MCD data were modeled by eq 3.[46]

$$\frac{\Delta\varepsilon}{E} = \frac{\gamma}{4\pi S}\int_0^{\pi}\int_0^{2\pi}\sum_i N_i(l_z\langle S_z\rangle_i M_{xy}^{\mathrm{eff}} + l_y\langle S_y\rangle_i M_{xz}^{\mathrm{eff}} + l_x\langle S_x\rangle_i M_{yz}^{\mathrm{eff}})\sin\theta\,\mathrm{d}\theta\,\mathrm{d}\phi \quad (3)$$

A fit of the MCD intensity to eq 3 using the spin Hamiltonian parameters g_0, *D*, and *E* allowed for the M_{ij}^{eff} transition moments to be obtained for the transition being probed. These transition moments were used to obtain the % polarization in the *x*, *y*, and *z* directions using eq 4, shown for % *x* polarization. The % polarizations in the *y* and *z* directions are obtained from cyclic permutations of the indices of eq 4.[46]

$$\%x = 100 \times \left[\frac{(M_{xy}^{\mathrm{eff}}M_{xz}^{\mathrm{eff}})^2}{(M_{xy}^{\mathrm{eff}}M_{xz}^{\mathrm{eff}})^2 + (M_{xy}^{\mathrm{eff}}M_{yz}^{\mathrm{eff}})^2 + (M_{yz}^{\mathrm{eff}}M_{xz}^{\mathrm{eff}})^2}\right] \quad (4)$$

From this analysis, the VTVH MCD data for HPPD−NO taken at 21 700 cm^{-1} are 85% *z*-polarized (fit to the isotherms is included in Figure 3C). This is consistent with the assignment of this transition as NO^- to Fe^{III} d CT. The *z* polarization refers to the axial tensor of the ZFS, which is collinear with the $Fe-N^{NO}$ bond, and thus the NO^- to Fe^{III} d CT is polarized along this bond. For the HPPD−HPP−NO complex, the fit of the VTVH MCD data at 21 400 cm^{-1} (fit shown in Figure 3D) is 49% *z*-polarized and 51% *x,y*-polarized, reflecting a new interaction resulting from the binding of the α-keto acid substrate. Fits of the VTVH isotherms of the ligand field transitions give the same polarizations as their respective NO^- to Fe^{III} d charge transfer transitions (predominantly *z*-polarized for HPPD−NO and mixed polarization for HPPD−HPP−NO, Supporting Information Figure S4). The <5000 cm^{-1} transition in HPPD−HPP−NO can be fit with a range of polarizations between 88% and 47% *z*-polarized (Supporting Information Figure S5). A more definitive fit cannot be obtained due to the noise in the data; however, the lowest energy transition is no more *x,y*-polarized than the NO^- to Fe^{III} d CT transition at 21 400 cm^{-1}.

Table 1. Key Geometric Parameters for E−NO, E−αKA−NO, and Fe−EDTA−NO

	E−NO	E−αKA−NO	Fe−EDTA−NO
$Fe-N^{NO}$	1.76 Å	1.76 Å	1.78 Å[a]/1.76 Å[b]
N−O	1.17 Å	1.17 Å	1.10 Å/ 1.18 Å
Fe−N−O	147°	149°	156°/149°

[a] EXAFS parameters. [b] Computational parameters.

3.2. Computational − $\{FeNO\}^7$. To further evaluate the geometric and electronic structures of the $\{FeNO\}^7$ complexes, computational models have been studied. A previous study evaluated a number of different functional and basis set combinations to provide an experimentally validated rationale for the choice of computational parameters.[23] From this study, the BP86 functional with 10% Hartree−Fock exchange included, in combination with a split basis set consisting of triple-ζ on the Fe−N−O unit and double-ζ on the remaining atoms (for computational efficiency, hereafter referred to as Gen), proved to be the most consistent with experiment. Previous computational studies on αKA by other groups have used a combination of B3LYP and the LACVP basis set.[12,34,35] Further rationale for the current choice of functional and basis set will be presented below. There are a number of structural choices for the computational model of α-keto acid reactivity. To understand dioxygen reactivity for the broader family of α-keto acid-dependent dioxygenase mononuclear nonheme iron enzymes and for comparison to the computational studies in the literature, the results for α-ketoglutarate bound to a facial triad (abbreviated as E−αKA) are shown in the text. As indicated in the text, comparable results were obtained for HPPD−HPP−NO in the orientation used in previous studies[27,28] and are presented in the Supporting Information. To develop a mechanism general to this broad family of enzymes, the model has been truncated to include only first sphere residue interactions. A survey of available crystal structures does not reveal any additional conserved residues that could interact with with the NO or O_2 binding steps of the mechanism.[47]

The HPPD−NO complex was modeled using the three protein derived residues making up the facial triad (2His/1 carboxylate), 2 water ligands, and NO coordinated to Fe. The geometry-optimized computational model (E-NO) is shown in Supporting Information Figure S6A, and key geometric parameters are given in Table 1. The geometric structure shows a strong $Fe-N^{NO}$ bond at 1.76 Å (and an Fe−N−O angle of 147°), which defines the *z*-axis of the molecule. The geometric structure of the FeNO unit in E−NO is similar to both the experimental EXAFS and the geometry-optimized structure of

Fe−EDTA−NO (Table 1). Examination of the molecular orbital diagram (Supporting Information, Figure S6B, left) and boundary surface plots (Supporting Information Figure S7) shows two unoccupied α NO π^* and 5 unoccupied β Fe d orbitals. This electronic structure is consistent with the $Fe^{III}-NO^-$ description determined for Fe−EDTA−NO.[1] To model the HPPD−HPP−NO complex, the two water ligands of the E−NO complex were replaced by α-ketoglutarate (αKA) as described above.[47] This geometry-optimized computational model (E−αKA−NO) also shows a strong $Fe-N^{NO}$ bond (1.76 Å, Fe−N−O angle of 149°), which again defines the z-axis of the molecule (Figure 4A and Table 1).[48] The electronic structure of the Fe−NO unit of E−αKA−NO is very similar to that of E−NO (molecular orbital diagram in Figure 4B, right and boundary surface plots in Figure 5). The αKA moiety has two molecular orbitals (the HOMO and LUMO) that interact with the Fe center (Figure 6). The occupied αKA n orbital (the αKA HOMO) is primarily a lone pair on the carboxylate with some in-plane character on the carbonyl and will have a σ bonding interaction with the Fe d_{xy} and d_{x2-y2} orbitals. (Note that in the coordinate system in Figure 4A, y is in the Fe−N−O plane that bisects equatorial ligand−metal bonds, and therefore d_{x2-y2} is a d_π orbital with lobes bisecting the ligand bonds and d_{xy} is the d_σ orbital with its lobes along the ligand−metal bonds.) The unoccupied αKA π^* LUMO is mostly on the carbonyl with conjugation onto the carboxylate and will have a π interaction with the Fe d_{yz} and d_{xz} orbitals. In the E−αKA−NO complex, these αKA-based MOs are β117 (n) and β122 (π^*) in Figure 4B, right, and Figure 5.

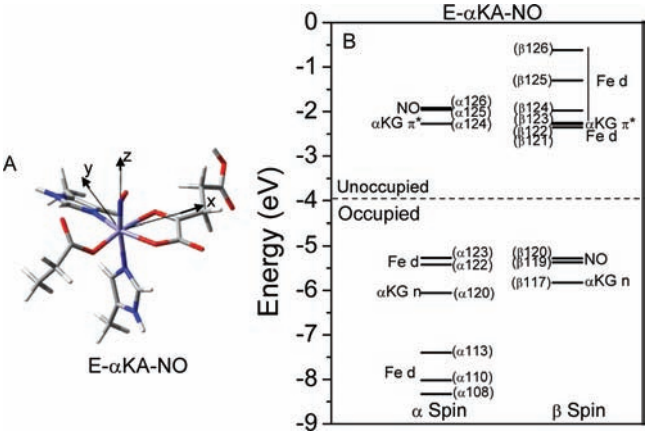

Figure 4. Computational model for $S = 3/2$ $\{FeNO\}^7$ E−αKA−NO. (A) Geometry-optimized structure and (B) molecular orbital diagram.

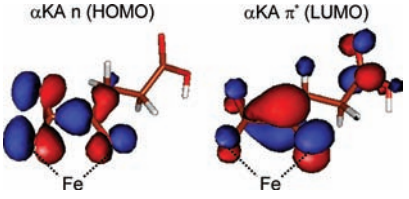

Figure 6. Boundary surface plots of αKA available for bonding to Fe.

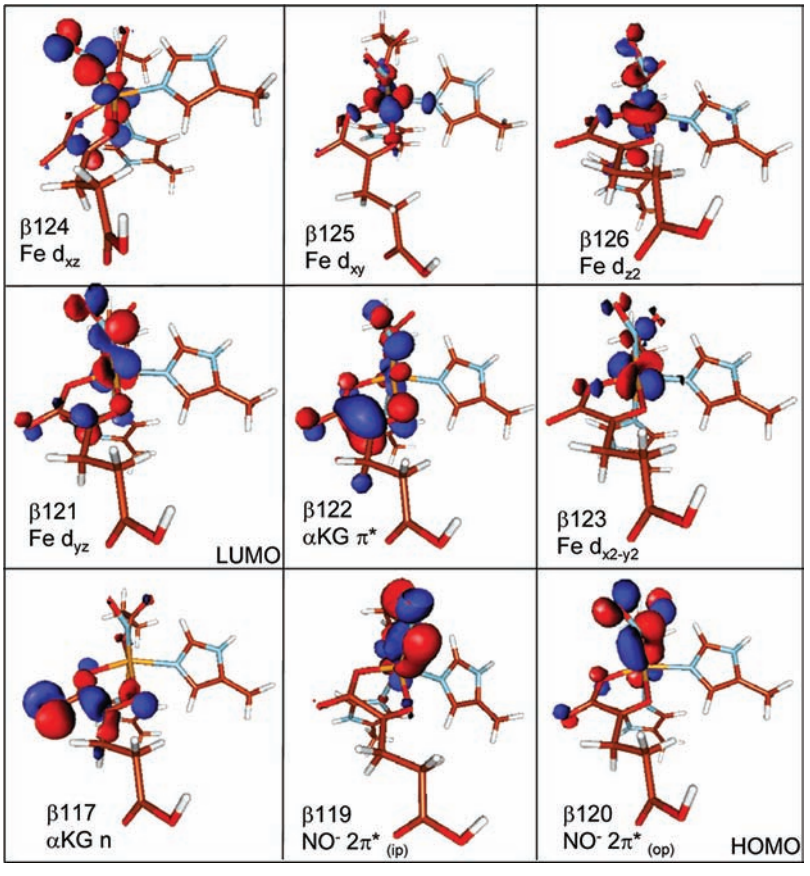

Figure 5. Select β boundary surface plots for the geometry-optimized structure of $S = 3/2$ E−αKA−NO.

dx.doi.org/10.1021/ja202549q | J. Am. Chem. Soc. 2011, 133, 18148–18160

4. ANALYSIS

4.1. Correlation of Calculations to Experiment. Using the geometry-optimized computational models E−NO and E−αKA−NO presented above, the effects of αKA binding on the experimental spectra were evaluated.

Time-dependent density functional theory (TD-DFT) was used to generate a predicted absorption spectrum for each computational model. The TD-DFT predicted absorption spectrum for the E−NO complex is shown in Figure 7A where the transitions with significant NO^- to Fe d character are modeled with Gaussian bandshapes with a width at half height of 3000 cm^{-1}. The primary transitions and their corresponding transition dipole moment directions are given in Table 2. The TD-DFT predicted absorption spectrum for the E−αKA−NO complex is shown in Figure 7B.[49] Binding of the αKA ligand introduces new bands in the predicted spectrum with significant contributions from the αKA n to Fe d_{x2-y2} (d_π) transition. These are included in Figure 7B (teal). The TD-DFT calculation predicts these transitions to be higher in energy than the NO^- to Fe d transitions (Table 2). From this, the highest energy transition in the UV−vis absorption (and MCD) spectrum of HPPD−HPP−NO is assigned as an αKA n to Fe d_{x2-y2} CT transition. Overlays of the experimental absorption and calculated TD-DFT spectra for HPPD−NO and HPPD−HPP−NO are in reasonable agreement and are shown in Supporting Information Figure S11.

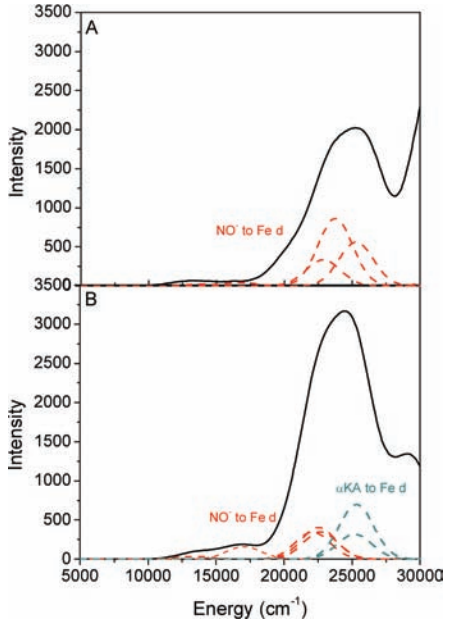

Figure 7. TD-DFT predicted absorption spectra. Plots of E−NO (A) and E−αKA−NO (B) predicted absorption spectra with Gaussian bandshapes with a width at half height of 3000 cm^{-1} shown for transitions with NO^- to Fe d (red) and αKA to Fe d (teal) charge transfer character.

The assignment of the new high energy transition in the absorption/MCD spectra to an αKA n to Fe d CT transition provides insight into the mixed polarization observed in the VTVH MCD data of the HPPD−HPP−NO. From the calculated transition dipole moment directions given in Table 2, the NO^- to Fe d CT transitions in E−NO are predominantly polarized in the *z* direction. This polarization direction refers to the axis of the ZFS and is consistent with the strong $Fe-N^{NO}$ bond, which defines the *z*-axis of the system. For the predicted E−αKA−NO complex NO^- to Fe d CT transitions, however, there is an *x,y* component of the transition dipole moment leading to an off axis transition moment direction. This reflects mixing with the αKA n to Fe d transition that has a transition dipole moment dominantly in the *x,y* direction (Table 2) consistent with αKA binding in the equatorial plane. The two charge transfer transitions are close in energy and mix through configuration interaction either through orbital overlap to generate the off axis transition dipole moment calculated or through SOC to give the mixed polarization observed in the VTVH MCD data.

The lower energy transitions in the MCD spectra of $\{FeNO\}^7$ complexes are assigned as the formally spin-forbidden Fe^{III}, ligand field transitions. As the TD-DFT calculations only give the spin-allowed transitions, ΔSCF calculations were undertaken to probe the energies of the specific Fe^{III} ligand field transitions. As promotion of a full electron resulted in wave functions that would not converge, these transitions were calculated as Slater transition states.[50] Table 3 gives the calculated transition energies for the Fe^{III} αd_σ to βd_π ligand field transitions.[51] From Table 3, for most of the ligand field transitions, the energies change only slightly between the E−NO and E−αKA−NO complexes. The most notable exception lies in the lowest energy, Fe^{III} αd_{z2} to βd_{x2-y2}, transition, which increases by ∼3800 cm^{-1} upon binding of αKA. This change is consistent with the appearance of a new band in the low energy region of the HPPD−HPP−NO MCD spectrum in Figure 3B; this transition would then be at still lower energy in the HPPD−NO MCD spectrum (below our

Table 3. ΔSCF Fe^{III} Spin-Forbidden Ligand Field Transition Energies

transition	E−NO	E−αKA−NO
$d_{z2}-d_{x2-y2}$	3600 cm^{-1}	7400 cm^{-1}
$d_{xy}-d_{x2-y2}$	8000 cm^{-1}	8700 cm^{-1}
$d_{xy}-d_{yz}$	12 500 cm^{-1}	12 500 cm^{-1}
$d_{z2}-d_{xz}$	14 100 cm^{-1}	14 800 cm^{-1}
$d_{xy}-d_{xz}$	16 100 cm^{-1}	19 100 cm^{-1}

Table 2. TD-DFT Transition Energies and Directions of Transition Dipole Moments

transition	experiment HPPD−NO	HPPD−HPP−NO	calculated E−NO	E−αKA−NO
$NO^- \rightarrow$ Fe d	19 500 cm^{-1}	17 600 cm^{-1}	13 900 cm^{-1}; *z*	13 500 cm^{-1}; *z*
	20 800 cm^{-1}	19 800 cm^{-1}	16 600 cm^{-1}; *x,y*/*z*[a]	17 500 cm^{-1}; *x,y*/*z*
	22 100 cm^{-1}[b]	22 000 cm^{-1}[b]	23 700 cm^{-1}; *z*[b]	22 000 cm^{-1}; *x,y*/*z*[b]
αKA n → Fe d		∼30 000 cm^{-1}		25 500 cm^{-1}; *x,y*

[a] Transition is mixed with a His→Fe CT transition. These His CT transitions are calculated to be significantly lower in energy than would be seen experimentally. [b] The polarization of this transition can be measured experimentally to compare to the direction of the transition dipole moment. HPPD−NO 85% *z* (exp), E−NO 89% *z* (calc); HPPD−HPP−NO 51% *x,y* and 49% *z* (exp), E−αKA−NO 70% *x,y* and 30% *z* (calc).

Table 4. NO^- $2\pi^*$ Character in Fe d_{yz} and d_{xz}

orbital	E−NO	E−αKA−NO
d_{yz}	24%	22%
d_{xz}	48%	32%
total	72%	54%

5000 cm^{-1} cutoff), and moved up in energy with αKA binding. As mentioned previously, the Fe^{III} ligand field transitions are formally spin-forbidden. These transitions become allowed through metal-based spin−orbit coupling (SOC) with the nearby spin-allowed charge transfer transitions. (For a more in-depth description of the SOC mechanism, see the Supporting Information.)

The increase in energy of this Fe^{III} d_{z2} to d_{x2-y2} transition (axes in Figure 4A and Supporting Information Figure S6A) upon binding of αKA reflects either a decrease in the energy of Fe d_{z2} or an increase in the energy of the d_{x2-y2} orbital. Alignment of the MO energy levels to the highest occupied NO^- orbital (Supporting Information Figure S12) shows that d_{z2} does not significantly change in energy between the E−NO and E−αKA−NO complexes (in fact, it increases in energy). This is consistent with the similar $Fe-N^{NO}$ bond lengths in the geometry-optimized structures and reflects the strong σ interaction of the NO with Fe d_{z2}. However, d_{x2-y2} increases in energy with addition of αKA, which reflects the addition of a much stronger donor ligand in the equatorial plane than the two water ligands it replaces from the E−NO complex. Note that even this BP86 + 10% HF exchange calculation does not fully account for the charge donation of the α-keto acid. While the calculation correctly predicts the shift up in energy of the lowest energy Fe^{III} ligand field transition due to donation by the α-keto acid, it does not predict the observed shift down in energy of the ∼12 000−13 000 cm^{-1} ligand field transition. Additionally, the αKA to Fe^{III} transition at ∼29 000 cm^{-1} is significantly more intense in the experimental absorption spectrum than in the corresponding TD-DFT predicted spectrum, supporting the assignment of αKA as a strong donor ligand, but again suggesting that the strength of the αKA donation is underestimated in these calculations. Quantitatively, the amount of αKA present in the unoccupied valence orbitals of the NO complex (relative to the amount of O from the waters it replaces) gives the relative donor strength. These values are 23% for αKA relative to 10% for the water ligands (from Mulliken population analyses). Assignment of the αKA moiety as a strong donor ligand has important implications for O_2 reactivity.

The axial ZFS parameter, D, obtained from fitting the temperature dependence of the $S = 3/2$ EPR signal (Supporting Information Figure S1) decreases by one-half in the αKA bound FeNO complex (from 16.0 to 8.4 cm^{-1}). This is reproduced in the DFT calculations where the ZFS parameters calculated using the optimized geometries for E−NO and E−αKA−NO (both calculated to be axial with z along $Fe-N^{NO}$) decrease from 10 to 6.6 cm^{-1}. Rodriquez et al. have evaluated the origin of the large ZFS in $S = 3/2$ $\{FeNO\}^7$ complexes (for Fe−[Me_3TACN]−$(N_3)_2$−NO where $D = 22$ cm^{-1}).[52] They attribute the large value of the ZFS to delocalization of electron density from the NO^- into the Fe d_{yz} and d_{xz} orbitals, which strongly overlap in the $\{FeNO\}^7$ unit. From Table 4, the amount of NO^- character in the β Fe d_{yz} and d_{xz} molecular orbitals does in fact decrease from 72% to 54% upon binding of αKA. This reflects the competition from the strong donation of the αKA into the d_π orbitals. Thus, the high energy CT feature in absorption/MCD, the mixed polarization from the VTVH MCD isotherms, the new low energy LF band in MCD, and the decreased value of D all reflect the strong donation of the αKA ligand to the Fe^{III}.

4.2. Comparison to B3LYP/LACVP. Most calculations published on the reactivity of α-keto acid-dependent mononuclear nonheme Fe complexes used the B3LYP/LACVP combination of functional and basis set.[12,34,35] Therefore, it was useful to evaluate its performance with respect to these experimental data. Geometry optimization of the E−NO and E−αKA−NO complexes with B3LYP/LACVP results in structures with $Fe-N^{NO}$ bond lengths ∼0.3 Å longer than the structures optimized with BP86 + 10%HF/Gen (Supporting Information Figure S13 and Table S2). This long $Fe-N^{NO}$ bond results in less electron density transferred to NO giving electronic structures, which are best described as $Fe^{II}-NO^{\bullet}$ (4 unoccupied β Fe d orbitals, 2 unoccupied α NO orbitals, and 1 unoccupied β NO orbital shown in the energy level diagram in Supporting Information Figure S14). The TD-DFT predicted absorption spectra of these complexes show a large change upon binding αKA (Supporting Information Figure S15), and the TD-DFT calculations also predict transitions that are predominantly Fe d to NO in character, consistent with the initial electronic structure description as $Fe^{II}-NO^{\bullet}$. This calculated large change in the TD-DFT predicted absorption spectrum upon binding αKA is not consistent with the observed experimental data (compare Figure 2 to Figure S15). Using the B3LYP/LACVP-optimized structures and the "spectroscopic parameters" basis set (CP(PPP) on Fe) with the B3LYP functional to calculate the ZFS gives values of D that are negative and E/D values that are significantly rhombic (Supporting Information Table S2). These are also not consistent with the experimentally observed strongly axial EPR signals with positive values of D (in Figure 1).

Finally, the free energy of NO binding to a resting, facial triad enzyme complex can be extracted from the known dissociation constant for NO binding to metapyrochatecase[53] and compared to the energies for the E−NO computational models. (In metapyrocatechase, the Fe center is also ligated by the facial triad, 2 water ligands, and NO, and the resulting complex has an $S = 3/2$ ground state.) The experimentally derived free energy of NO binding is ∼ −4.4 kcal/mol, while the calculated values for the two model systems are −4.9 kcal/mol for BP86 + 10%/Gen and +9.4 kcal/mol for B3LYP/LACVP (T = 298 K, solvation − ε = 4.0). Thus, the calculated NO binding energy for B3LYP/LACVP predicts that the E−NO complex is not stable, which is inconsistent with experiment.

Thus, two different computational methods produce different electronic structures. The spectroscopic data support the choice of BP86 + 10%/Gen as an experimentally calibrated computational model to best evaluate the NO complex and by extension the O_2 complex. The difference between these two electronic structures reflects the extent of charge donation from Fe to NO, which will have implications on the interactions of O_2 with the Fe center in the evaluation of the O_2 reaction coordinate to form the Fe^{IV}═O species.

4.3. Extension to $\{FeO_2\}^8$. On the basis of the above analysis, the BP86 + 10%HF/Gen computational approach was used to evaluate the $\{FeO_2\}^8$ complex and the reaction coordinate of αKA-dependent dioxygenases. The free energy of O_2 binding to the E computational model in this study is 17 kcal/mol (T = 298 K, solvation − ε = 4.0), consistent with the previous

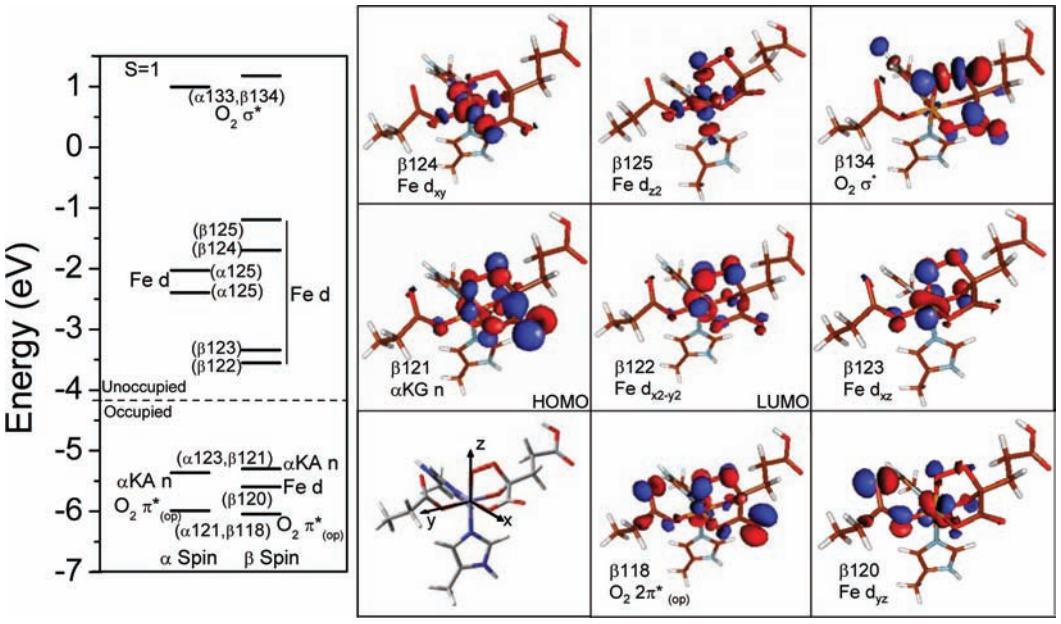

Figure 8. Molecular orbital diagram (left) and select β boundary surface plots (right) for geometry-optimized structure of $S = 1$ E$-\alpha$KA$-$O$_2$. Optimized structure is shown in the lower left corner. Selected bond lengths are given in Table 5.

Table 5. Key Geometric and Electronic Structure Parameters for E$-\alpha$KA$-$O$_2$ Complexes

	$S = 3$	$S = 2$	$S = 1$
Fe$-$O	2.18 Å	2.06 Å	1.80 Å
O$-$O	1.28 Å	1.28 Å	1.41 Å
Fe$-$O$-$O	118.0°	118.5°	110.3°
electronic structure	$Fe^{III}-O_2^{\bullet-}$	$Fe^{III}-O_2^{\bullet-}$	$Fe^{IV}-O_2^{2-}$
ΔG O$_2$ binding[a]	12.0 kcal/mol	12.5 kcal/mol	5.8 kcal/mol

[a] $T = 298$ K; solvation $-$ $\varepsilon = 4.0$.

computational study of $\Delta G^{\ddagger}$ of 22 kcal/mol for the resting form of metapyrocatechase and the fact that the holoenzyme does not react with O$_2$ in the absence of αKA (or substrate in the case of metapyrocatechase).[54] To evaluate the $\{FeO_2\}^8$ complex, the NO of the E$-\alpha$KA$-$NO complex was replaced with O$_2$, and the structures for the different possible spin states were reoptimized.

The complex of O$_2$ ($S = 1$) bound to Fe^{II} ($S = 2$) can have a total spin of $S = 3$, $S = 2$, $S = 1$, or $S = 0$. Dioxygen binding in each of these spin states was evaluated.[55] The geometry-optimized structures and MO diagrams for the E$-\alpha$KA$-$O$_2$ complexes are shown in Figure 8 and Supporting Information Figures S16,17, with key geometric parameters given in Table 5. The $S = 3$ E$-\alpha$KA$-$O$_2$-optimized structure (end-on) is best described as a Fe^{III} ferromagnetically coupled to $O_2^{\bullet-}$ (5 unoccupied β Fe d orbitals and 1 unoccupied β O$_2$ π^* orbital, Supporting Information Figure S17, left). The optimized E$-\alpha$KA$-$O$_2$ structure in the $S = 2$ spin state is again end on and best described as a high spin Fe^{III} antiferromagnetically coupled to $O_2^{\bullet-}$ (5 unoccupied β Fe d orbitals and 1 unoccupied α O$_2$ π^* orbital, Supporting Information Figure S17, right, and Supporting Information Figure S18 for boundary surface plots). For the $S = 1$ E$-\alpha$KA$-$O$_2$ complex, the lowest energy structure is a new bridged binding mode to the αKA ligand (Figure 8, right $-$ bottom left corner). This structure is best described as a low spin $Fe^{IV}-O_2^{2-}$ (4 unoccupied β Fe d orbitals and 2 unoccupied α Fe d orbitals, Figure 8, left, with boundary surface plots in Figure 8, right). Comparison of the free energy of O$_2$ binding for each spin state (Table 5) reveals the $S = 1$ bridged binding mode is significantly lower in energy than the $S = 2$ and $S = 3$ spin states.[56] Consistent with the endergonic nature of the O$_2$ binding, no O$_2$ bound species is observed prior to the formation of the Fe^{IV}=O intermediate.[14]

A linear transit calculation was used to evaluate O$_2$ binding to form the new peroxide bridged binding mode (Figure 9 and Table 6). At long Fe$-$O$_2$ distances, an $S = 1$ description of the E$-\alpha$KA$-$O$_2$ complex starts as an antiferromagnetic coupled E$-\alpha$KA (Fe^{II}, $S = 2$) and O$_2$ ($S = 1$) system (Figure 9, left). As the O$_2$ approaches the Fe^{II} E$-\alpha$KA complex, charge is transferred from Fe to O$_2$, resulting in more ferric character. This increases the interaction with the αKA resulting in shorter Fe$-$O$^{\alpha KA}$ bonds that increases the ligand field at the iron center resulting in an E$-\alpha$KA$-$O$_2$ complex that is a low spin, ferromagnetically coupled $Fe^{III}-O_2^{\bullet-}$ species (Figure 9, step 1). Further interaction of the superoxide with the Fe center leads to transfer of a second electron to form an $Fe^{IV}-O_2^{2-}$ species (Figure 9, step 2). To form the bridge, the occupied O_2^{2-} $\pi^*_{(ip)}$ orbital has a nucleophilic interaction with the unoccupied αKA π^* orbital (Scheme 3) forming a σ bond between the distal O of the peroxide and the carbonyl carbon of the αKA.

This structure is of interest as a potential intermediate for study experimentally. Although based on the equilibrium between the unbound O$_2$ and peroxy-bridged structures the population of peroxy-bridged species will be small, there is still a barrier after formation of the peroxo-bridged structure (vide infra). The TD-DFT predicted absorption spectrum was calculated to evaluate where the peroxo to Fe charge transfer transitions are expected. This calculated spectrum with Gaussian broadening of the peroxo to Fe CT transtions is shown in Supporting Information Figure S19. An $Fe^{IV}$$-$alkylperoxo model complex has been reported by Que and co-workers.[57] The TD-DFT calculated

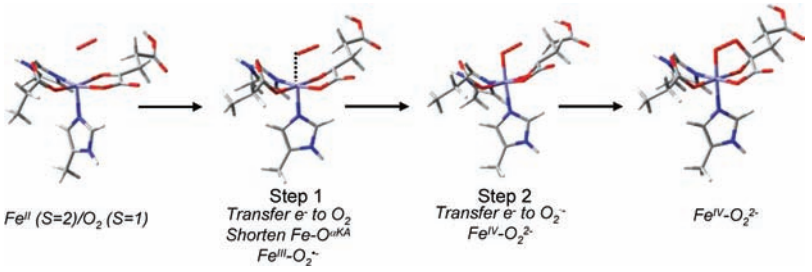

Figure 9. Formation of $S = 1$ $Fe^{IV}-O_2^{2-}$ bridge. Four points along formation of $S = 1$ $Fe^{IV}-O_2^{2-}$ bridge structure: initial $Fe^{II}-O_2$ (left, Fe– O = 2.50 Å), step 1 (middle left, Fe– O = 2.10 Å), step 2 (middle right, Fe– O = 1.90 Å), and bridged $Fe^{IV}-O_2^{2-}$ (right).

Table 6. Steps To Form the $S = 1$ Peroxo-Bridged Structure

	approach	step 1	step 2	bridged structure
Fe–O	2.50 Å	2.10 Å	1.90 Å	1.80 Å
O–O	1.23 Å	1.30 Å	1.34 Å	1.41 Å
O–C	3.15 Å	1.90 Å	1.70 Å	1.47 Å
$Fe-O^{CO}$	2.31 Å	1.91 Å	1.88 Å	1.84 Å
$Fe-O^{CO2}$	2.02 Å	1.90 Å	1.90 Å	1.89 Å
Fe–O–O	120.0°	111.7°	112.2°	110.3°
$Fe-O^{CO}-C-C$	5.2°	39.4°	48.5°	55.8°
relative electronic energy	0.0 kcal/mol	−9.5 kcal/mol	−15.2 kcal/mol	−19.4 kcal/mol
electronic structure	$Fe^{II}-O_2$	$Fe^{III}-O_2^{\bullet-}$ (low spin)	$Fe^{IV}-O_2^{2-}$	$Fe^{IV}-O_2^{2-}$

Scheme 3. Nucleophilic Interaction between the Occupied O_2^{2-} $\pi^*_{(ip)}$ Orbital and the Unoccupied αKA π^* Orbital

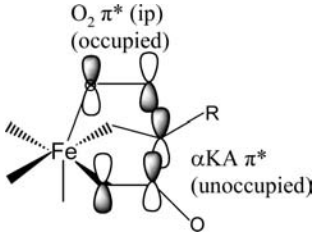

absorption spectrum in Figure S19 is in good agreement with the experimental absorption spectrum of this complex and strengthens their assignment of the two lowest energy transitions as peroxo to Fe^{IV} CT.

4.4. Completion of α-Keto Acid-Dependent Nonheme Iron Reaction Coordinate. The first experimentally observed intermediate for the α-keto acid-dependent dioxygenases is an Fe^{IV}═O, which has an $S = 2$.[14,58,59] From the low spin $Fe^{IV}-O_2^{2-}$ $S = 1$ structure in Figure 8, a spin intersystem crossing must occur to allow the reaction coordinate to proceed on the $S = 2$ surface. Cleavage of both the C–C (to release CO_2) and the O–O bonds occurs before formation of the Fe^{IV}═O species. Changing the O–O coordinate increases the energy of both spin states (Supporting Information Figure S20). However, on the C–C coordinate, the two spin states cross in energy, and this coordinate was pursued. Intersystem crossing on the C–C coordinate requires that the two spin surfaces have a similar energy and geometry (minimum energy crossing point, MECP), and their electronic structures should differ by one electron on the same center, such that the two states can spin orbit couple. The optimizations of the bridged O_2 structure in both the $S = 1$

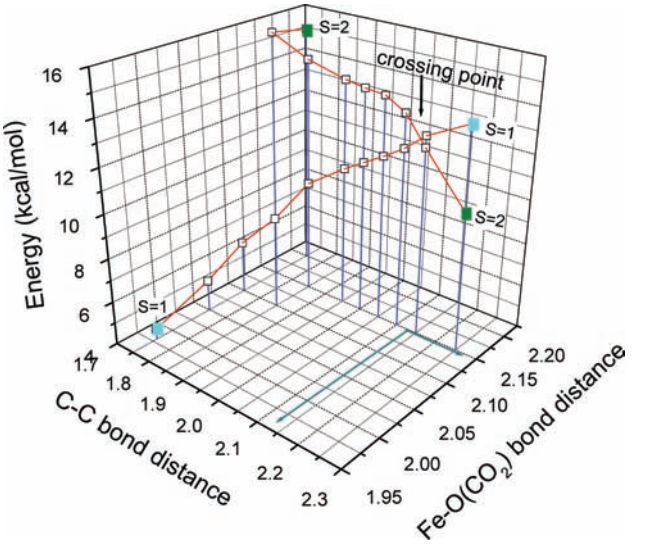

Figure 10. 2-D spin crossover surface. Electronic energies for elongation of C–C while decreasing the difference in $Fe-O^{CO2}$ bond length. The energies of the two spin states cross at an $Fe-O^{CO2}$ distance of 2.15 Å and a C–C bond length of 2.10 Å. For clarity, only the minimum energy points are shown; however, points were taken at C–O bond distances on either side of the minimum energy points. The energies are relative to the optimized $S = 1$ bridged structure.

and the $S = 2$ spin states show that the geometries are very similar with the exception of the $Fe-O^{CO2}$ distance (which is 1.93 Å in $S = 1$ and 2.30 Å in $S = 2$). Thus, a 2-D potential energy scan (elongation of the C–C bond while decreasing the difference between the $Fe-O^{CO2}$ bond lengths) was evaluated to find the spin surface crossing point (Figure 10). A crossing point in the energies was found at a C–C bond length of ~2.1 Å.

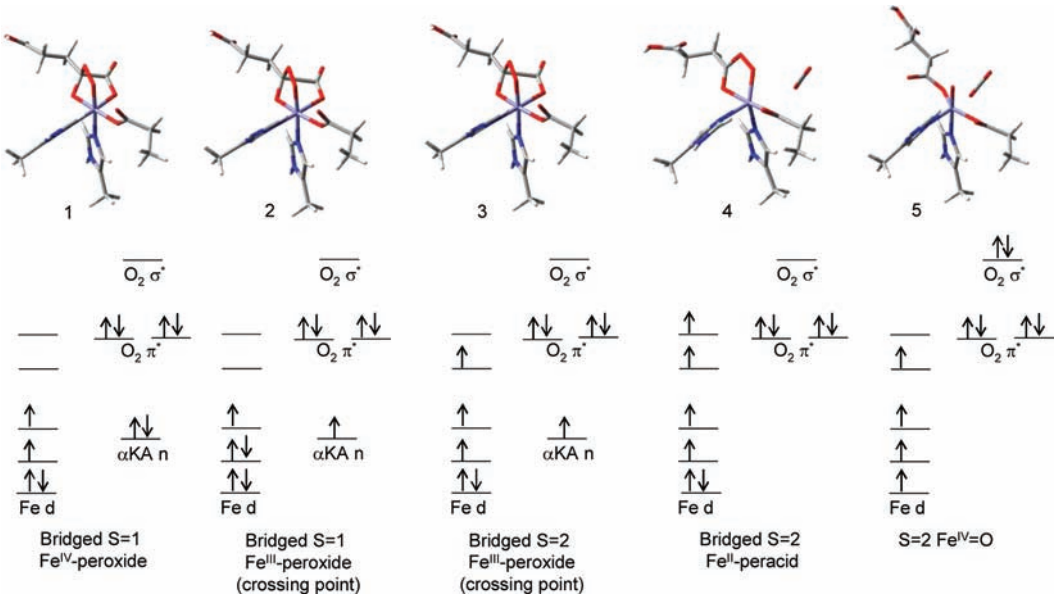

Figure 11. Electron flow for steps of E−αKA−O_2 reaction to form Fe^{IV}=O, $S = 2$. Dioxygen binding occurs on the $S = 1$ surface with formation of a bridge to the α-keto acid moiety. Two electrons are transferred to the O_2 π^* orbital generating a low spin Fe^{IV}−peroxide (1). Elongation of the C−C bond results in transfer of 1e$^-$ from the αKA n orbital to form an Fe^{III}−peroxide, which crosses over to the $S = 2$ surface (2,3). Once on the $S = 2$ surface, the second electron of the αKA n orbital is transferred to Fe, generating an Fe^{II}−peracid and free CO_2 (4). Finally, cleavage of the O−O bond leads to formation of an Fe^{IV}−oxo $S = 2$ (5).

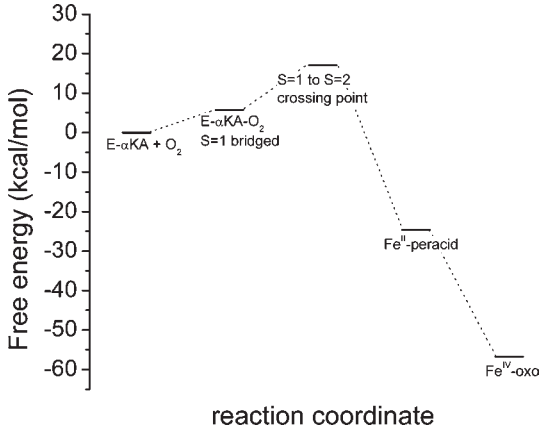

Figure 12. Free energy diagram for initial steps of E−αKA−O_2 reaction ($T = 298$ K; solvation − $\varepsilon = 4.0$).

The electronic structures of the $S = 1$ and $S = 2$ models (Figure 11, structures 2 and 3) are both Fe^{III}−O_2^{2-}, where as the C−C was elongated, one e$^-$ transferred from the αKA n orbital to the Fe (Supporting Information Figure S21). The $S = 1$ and $S = 2$ states at this MECP differ by one e$^-$: occupied β Fe d_{xz} and α Fe d_{z^2}[60] (Figure 11, structures 2 and 3). Thus, these two states SOC via L_y (Supporting Information Figure S22).[60,61]

Once on the $S = 2$ surface, the C−C bond cleaves without any additional barrier and transfers the second αKA n electron to Fe forming a high spin Fe^{II}−peracid (Figure 11, structure 4). The transfer of 2 e$^-$'s from Fe^{II} into the peracid σ^* orbital to break the O−O bond is accomplished with a minimal additional barrier (calculated <1 kcal/mol) to form the experimentally observed $S = 2$ Fe^{IV}=O. The free energies for these steps of the O_2 reaction are given in Figure 12. The reaction of the Fe^{IV}−oxo with substrate in HPPD has been evaluated in ref 28.

5. DISCUSSION

The comparison of the NO complexes of HPPD and HPPD−HPP provides a probe of the new spectral features that arise from the α-keto acid bonding to the ferric site. Four new spectral features are observed in the HPP bound HPPD−NO complex that reflect a new electronic structure: a new αKA to Fe^{III} charge transfer transition above 25 000 cm^{-1} in the UV−vis absorption and MCD spectra, mixed polarization of the NO$^-$ to Fe^{III} charge transfer bands, a new low energy, ligand field MCD transition at <5000 cm^{-1}, and a decrease by one-half in the ZFS. The new charge transfer transition reflects the donor interaction of the α-keto acid ligand to the Fe^{III}. The <5000 cm^{-1} ligand field band in the HPPD−HPP−NO complex also reflects the strong equatorial donor interaction of the α-keto acid with the $\{FeNO\}^7$ unit, which further leads to the decrease in the ZFS. Taken together, these spectroscopic changes indicate that the α-keto acid ligand is a strong donor that promotes increased charge transfer from Fe^{III} to NO$^-$.

Replacement of NO with O_2 in calculations that reproduce the α-keto acid−$\{FeNO\}^7$ spectral features results in a new, low energy $S = 1$ peroxy-bridged structure. Charge donation from iron to O_2 results in increased ferric character that increases the bonding and donation of the α-keto acid ligand,[62] which promotes formation of this low spin Fe^{IV}−peroxide bridge (Figure 9). As the experimentally observed Fe^{IV}=O product of O−O cleavage has an $S = 2$ ground state, the $S = 1$ bridged peroxide must cross over to the $S = 2$ surface to form the Fe^{IV}=O species. A minimum energy crossing point from the $S = 1$ to $S = 2$ surface along the C−C coordinate (C−C = 2.10 Å) was found. The free energy to this step is ~17 kcal/mol (Figure 12, starting from the reaction of E−αKA with dioxygen, $T = 298$ K, solvation − $\varepsilon = 4.0$), which is in reasonable agreement with experiment ($\Delta G^{\ddagger} \approx 14$ kcal/mol).[14,58,59] Thus, a bridged Fe^{IV}−peroxide binding mode is a viable step along the α-keto acid-dependent

mononuclear nonheme Fe−O_2 reaction coordinate. From this S = 2 peroxy species, decarboxylation occurs, and the resultant Fe^{II}−peracid undergoes O−O cleavage to give the Fe^{IV}=O species with a minimal (<1 kcal/mol) barrier.

Previous studies, using the B3LYP/LACVP approach, suggested that an $S = 2$ $Fe^{III}-O_2^{\bullet-}$ species initiates the reaction with α-keto acids.[12,34,35] However, this functional/basis set combination generates structures with long $Fe-O^{O2}$ bonds and less charge transfer from Fe to O_2 (i.e., less Fe^{III} character), which in turn results in less donor bonding by the αKA and prevents the formation of a low energy peroxy bridged structure. In this study, the experimentally validated computational methods lead to αKA binding as a strong donor ligand (from experiment) that drives the formation of the S = 1, low spin bridged Fe^{IV}−peroxide intermediate.

As triplet O_2 approaches the Fe^{II}, orbital overlap would lead to antiferromagnetic coupling to give the S = 1 surface. Continuing along the S = 1 surface leads to the S = 1 Fe^{IV}−peroxide intermediate that can nucleophilically attack the α-keto acid π^* LUMO on the carbonyl. This intermediate (not present in B3LYP/LACVP calculations[12,34,35]) has been postulated since early studies of α-keto acid-dependent mononuclear nonheme iron enzymes,[10] but had not been validated until now. Finally, the effect, elucidated in this study, associated with the binding of a strong donor ligand (i.e., αKA) on the initial dioxygen activation steps likely has implications for the mechanisms of other nonheme Fe^{II} oxygen activating enzymes in which the substrate or cofactor binds directly to the metal center.

■ ASSOCIATED CONTENT

Supporting Information. Full ref 30; description of SOC mechanism; key geometric and electronic structure parameters for HPPD−HPP−NO and for E−NO and E−αKA−NO with different functionals; temperature-dependent EPR data with fits; Fe−EDTA−NO UV−vis abs and MCD spectra; VTVH MCD isotherms and fits for LF transitions; computational models and molecular orbital diagrams for E−NO, HPPD−HPP−NO, E−αKA−NO + salt bridge, and S = 2 and S = 3 E−αKA−O_2; comparison of energies of Fe d_π orbitals; TD-DFT comparisons for different models, to experimental data, for the S = 1 peroxo-bridged structure; geometric and electronic structure comparison between B3LYP/LACVP and BP86 + 10%HF/Gen computational models; boundary surface plots for E−NO and S = 2 E−αKA−O_2; spin crossover 2D-PES, molecular orbital diagrams, and SOC; and Cartesian coordinates for stationary structures. This material is available free of charge via the Internet at http://pubs.acs.org.

■ AUTHOR INFORMATION

Corresponding Author
edward.solomon@stanford.edu

■ ACKNOWLEDGMENT

This research was supported by NIH Grant GM40392 (E.I.S.) and NSF Grant MCB0843619 (G.R.M.). We would like to thank Dr. Martin Srnec for assistance in performing calculations.

■ REFERENCES

(1) Solomon, E. I.; Brunold, T. C.; Davis, M. I.; Kemsley, J. N.; Lee, S. K.; Lehnert, N.; Neese, F.; Skulan, A. J.; Yang, Y. S.; Zhou, J. *Chem. Rev.* **2000**, *100*, 235–349.
(2) Neidig, M. L.; Solomon, E. I. *Chem. Commun.* **2005**, *47*, 5843–5863.
(3) Purpero, V.; Moran, G. R. *J. Biol. Inorg. Chem.* **2007**, *12*, 587–601.
(4) Hausinger, R. P. *Crit. Rev. Biochem. Mol. Biol.* **2004**, *39*, 21–68.
(5) Hegg, E. L.; Que, L., Jr. *Eur. J. Biochem.* **1997**, *250*, 625–629.
(6) Koehntop, K. D.; Emerson, J. P.; Que, L., Jr. *J. Biol. Inorg. Chem.* **2005**, *10*, 87–93.
(7) Lange, S. J.; Que, L., Jr. *Curr. Opin. Chem. Biol.* **1998**, *2*, 159–172.
(8) van der Donk, W. A.; Krebs, C.; Bollinger, J. M., Jr. *Curr. Opin. Struct. Biol.* **2010**, *20*, 673–683.
(9) Schofield, C. J.; Zhang, Z. *Curr. Opin. Struct. Biol.* **1999**, *9*, 722–731.
(10) Hanauske-Abel, H. M.; Günzler, V. *J. Theor. Biol.* **1982**, *94*, 421–455.
(11) Bollinger, J. M., Jr.; Krebs, C. *J. Inorg. Biochem.* **2006**, *100*, 586–605.
(12) de Visser, S. P. *Coord. Chem. Rev.* **2009**, *253*, 754–768.
(13) Kovaleva, E. G.; Lipscomb, J. D. *Nat. Chem. Biol.* **2008**, *4*, 186–193.
(14) Price, J. C.; Barr, E. W.; Tirupati, B.; Bollinger, J. M., Jr.; Krebs, C. *Biochemistry* **2003**, *42*, 7497–7508.
(15) Arciero, D. M.; Lipscomb, J. D.; Huynh, B. H.; Kent, T. A.; Munck, E. *J. Biol. Chem.* **1983**, *258*, 4981–4991.
(16) Han, A. Y.; Lee, A. Q.; Abu-Omar, M. M. *Inorg. Chem.* **2006**, *45*, 4277–4283.
(17) Roach, P. L.; Clifton, I. J.; Hensgens, C. M. H.; Shibata, N.; Schofield, C. J.; Hajdu, J.; Baldwin, J. E. *Nature* **1997**, *387*, 827–830.
(18) Westcott, B. L.; Enemark, J. H. Transition Metal Nitrosyls. In *Inorganic Electronic Structure and Spectroscopy, Vol. II*; Solomon, E. I., Lever, A. P. B., Eds.; Wiley: New York, 1999.
(19) Yang, T. C.; Wolfe, M. D.; Neibergall, M. B.; Mekmouche, Y.; Lipscomb, J. D.; Hoffman, B. M. *J. Am. Chem. Soc.* **2003**, *125*, 7056–7066.
(20) Ye, S. F.; Price, J. C.; Barr, E. W.; Green, M. T.; Bollinger, J. M., Jr.; Krebs, C.; Neese, F. *J. Am. Chem. Soc.* **2010**, *132*, 4739–4751.
(21) Enemark, J. H.; Feltham, R. D. *Coord. Chem. Rev.* **1974**, *13*, 339–406.
(22) Brown, C. A.; Pavlosky, M. A.; Westre, T. E.; Zhang, Y.; Hedman, B.; Hodgson, K. O.; Solomon, E. I. *J. Am. Chem. Soc.* **1995**, *117*, 715–732.
(23) Schenk, G.; Pau, M. Y. M.; Solomon, E. I. *J. Am. Chem. Soc.* **2004**, *126*, 505–515.
(24) For these spin unrestricted, open shell systems, occupied orbitals are spin polarized to low energy and very mixed. For the bonding description generated here, we use the unoccupied antibonding orbitals to define the uncompensated occupied orbitals involved in bonding.
(25) Brown, C. D.; Neidig, M. L.; Neibergall, M. B.; Lipscomb, J. D.; Solomon, E. I. *J. Am. Chem. Soc.* **2007**, *129*, 7427–7438.
(26) Johnson-Winters, K.; Purpero, V. M.; Kavana, M.; Nelson, T.; Moran, G. R. *Biochemistry* **2003**, *42*, 2072–2080.
(27) Neidig, M. L.; Brown, C. D.; Kavana, M.; Choroba, O. W.; Spencer, J. B.; Moran, G. R.; Solomon, E. I. *J. Inorg. Biochem.* **2006**, *100*, 2108–2116.
(28) Neidig, M. L.; Decker, A.; Choroba, O. W.; Huang, F.; Kavana, M.; Moran, G. R.; Spencer, J. B.; Solomon, E. I. *Proc. Natl. Acad. Sci. U.S.A.* **2006**, *103*, 12966–12973.
(29) Neidig, M. L.; Kavana, M.; Moran, G. R.; Solomon, E. I. *J. Am. Chem. Soc.* **2004**, *126*, 4486–4487.
(30) Frisch, M. J.; et al. *Gaussian 03*, revision E.01; Gaussian, Inc.: Pittsburgh, PA, 2007.
(31) Perdew, J. P. *Phys. Rev. B: Condens. Matter Mater. Phys.* **1986**, *33*, 8822–8824.

(32) Becke, A. D. *Phys. Rev. A: At., Mol., Opt. Phys.* **1988**, *38*, 3098–3100.
(33) Cramer, C. J.; Truhlar, D. G. *Chem. Rev.* **1999**, *99*, 2161–2200.
(34) Borowski, T.; Bassan, A.; Siegbahn, P. E. M. *Chem.-Eur. J.* **2004**, *10*, 1031–1041.
(35) Borowski, T.; Bassan, A.; Siegbahn, P. E. M. *Biochemistry* **2004**, *43*, 12331–12342.
(36) *ADF2010.02*; SCM, Theoretical Chemistry, Vrije Universiteit: Amsterdam, The Netherlands, 2010; http://www.scm.com.
(37) Guerra, C. F.; Snijders, J. G.; te Velde, G.; Baerends, E. J. *Theor. Chem. Acc.* **1998**, *99*, 391–403.
(38) Velde, G. T.; Bickelhaupt, F. M.; Baerends, E. J.; Guerra, C. F.; Van Gisbergen, S. J. A.; Snijders, J. G.; Ziegler, T. *J. Comput. Chem.* **2001**, *22*, 931–967.
(39) Neese, F. *Inorg. Chim. Acta* **2002**, *337*, 181–192.
(40) Dennington, R., II; Keith, T.; Millam, J.; Eppinnett, K.; Hovell, W. L.; Gilliland, R. *GaussView, Version 3.09*; Semichem, Inc.: Shawnee Mission, KS, 2003.
(41) Tenderholt, A. L. *QMForge, Version 2.1*.
(42) Schaftenaar, G.; Noordik, J. H. *J. Comput.-Aided Mol. Des.* **2000**, *14*, 123–134.
(43) Gorelsky, S. I. *SWizard program*, 2010.
(44) Gorelsky, S. I.; Lever, A. B. P. *J. Organomet. Chem.* **2001**, *635*, 187–196.
(45) Abragam, A.; Bleaney, B. *Electron Paramagnetic Resonance of Transition Ions*; Oxford University Press: Oxford, 1970.
(46) Neese, F.; Solomon, E. I. *Inorg. Chem.* **1999**, *38*, 1847–1865.
(47) In the majority of available crystal structures of α-ketoglutarate-dependent dioxygenases with αKG bound, the free carboxylate tail of αKG is part of a salt bridge. Expansion of the model to include this salt bridge did not significantly affect the overall system (see Supporting Information Tables S1 and S8 and Figures S8,S9). For computational efficiency, calculations were done with a protonated carboxylate tail to neutralize the charge.
(48) The geometry-optimized structure, molecular orbital diagram, and key geometric parameters for the HPPD-derived models (HPPD−HPP−NO) are shown in Supporting Information Figures S8,S9 and Table S1.
(49) The overlaid TD-DFT predicted absorption spectra for E−αKA−NO and HPPD−HPP−NO are shown in Supporting Information Figure S10.
(50) Slater, J. C. *Quantum Theory of Atomic Structure*; McGraw-Hill: New York, 1960.
(51) The Slater transition state for the α d_{z2} to β d_{yz} transition in both complexes did not converge.
(52) Aquino, F.; Rodriguez, J. H. *J. Phys. Chem. A* **2009**, *113*, 9150–9156.
(53) Arciero, D. M.; Orville, A. M.; Lipscomb, J. D. *J. Biol. Chem.* **1985**, *260*, 4035–4044.
(54) Davis, M. I.; Wasinger, E. C.; Decker, A.; Pau, M. Y. M.; Vaillancourt, F. H.; Bolin, J. T.; Eltis, L. D.; Hedman, B.; Hodgson, K. O.; Solomon, E. I. *J. Am. Chem. Soc.* **2003**, *125*, 11214–11227.
(55) The S = 0 E−αKA−O_2 complex has spin expectation value close to 1, indicating significant spin contamination. Therefore, we have not pursued this spin state further.
(56) This is in contrast to the energy ordering with B3LYP/LACVP where an S = 1 O_2 end on geometry is lowest in energy and an S = 1 bridged binding mode is higher in energy by 22 kcal/mol (from ref 3434). (The S = 1 bridged binding mode is also an Fe^{III}−superoxo complex in contrast with the Fe^{IV}−peroxo obtained here.) These E−αKA−O_2-optimized structures in B3LYP/LACVP have a very long $Fe-O^{O2}$ interaction as was also found in section 4.2 for the E−αKA−NO complexes.
(57) Jensen, M. P.; Costas, M.; Ho, R. Y.; Kaizer, J.; Mairata i Payeras, A.; Munck, E.; Que, L., Jr.; Rohde, J. U.; Stubna, A. *J. Am. Chem. Soc.* **2005**, *127*, 10512–10525.
(58) Galonic, D. P.; Barr, E. W.; Walsh, C. T.; Bollinger, J. M., Jr.; Krebs, C. *Nat. Chem. Biol.* **2007**, *3*, 113–116.
(59) Hoffart, L. M.; Barr, E. W.; Guyer, R. B.; Bollinger, J. M., Jr.; Krebs, C. *Proc. Natl. Acad. Sci. U.S.A.* **2006**, *103*, 14738–14743.
(60) Movement toward the crossing point results in a weaker interaction along $N^{eq}-Fe-O^{CO2}$ and a tetragonal elongation of the site, which rotates the coordinate system such that the z-axis is along $N^{eq}-Fe-O^{CO2}$.
(61) Further elongation of the C−C bond on the S = 1 surface continues to be energetically unfavorable as there is no transfer of the second electron from the αKA n orbital (Supporting Information Figure S21). The S = 3 surface was also considered. However, at the crossing point, the S = 3 structure is 10 kcal/mol higher in energy than the S = 1 and S = 2 structures, making its involvement unlikely in this reaction.
(62) The αKA donation relative to the O_{water} it replaces can again be estimated from their relative character in the unoccupied valence orbitals in the FeO_2 complexes, which are 38% αKA versus 11% O of the 2 water molecules (from Mulliken population analyses).